

Disentangling morphology and conductance in amorphous graphene

Nicolas Gastellu¹, Ata Madanchi², Lena Simine^{1,2*}

¹Department of Chemistry, McGill University, Montréal & H3A 0B8, Canada.

²Department of Physics, McGill University, Montréal & H3A 2T8, Canada.

*Corresponding author. Email: lena.simine@mcgill.ca

Amorphous graphene or amorphous monolayer carbon (AMC) is a family of carbon films that exhibit a surprising sensitivity of electronic conductance to morphology. We combine deep learning-enhanced simulation techniques with percolation theory to analyze three morphologically distinct mesoscale AMCs. Our approach avoids the pitfalls of applying periodic boundary conditions to these fundamentally aperiodic systems or equating crystalline inclusions with conducting sites. We reproduce the previously reported dependence of charge conductance on morphology and explore the limitations of partial morphology descriptors in witnessing conductance properties. Finally, we perform crystallinity analysis of conductance networks along the electronic energy spectrum and show that they metamorphose from being localized on crystallites at band edges to localized on defects around the Fermi energy opening the possibility of control through gate voltage.

One sentence summary Modeling of atomically resolved mesoscale amorphous graphene unveils a tunable disorder-conductance relationship.

Understanding the role of microscopic structure in determining the macroscopic prop-

erties of a material is an important overarching goal in chemistry, physics, and molecular engineering. Of particular interest is establishing structure-function relationships for materials classified as “amorphous”. Although the adjective “amorphous” may suggest that the structure is simply a random arrangement of atoms, it is well known that the properties of real amorphous materials sensitively depend on the preparation route (deposition rates, temperature of substrate, etc.) implying configurational tunability at the atomic-level. The rich chemical and conformational landscapes of these materials pose many challenges to theory and experiment, and drive innovation in both (1).

Disorder inherent in amorphous materials is difficult to control and characterize experimentally and it is hard to replicate in a simulation (1). Amorphous graphene, or amorphous monolayer carbon (AMC) has recently emerged as a uniquely suitable model system for studying structure-function relationships in amorphous materials (2). Thanks to the two-dimensional configuration which can be visualized using microscopy and to the conjugated-carbon composition that is relatively easy to model computationally the correspondence between simulation and experiment can be established precisely. In recent years AMCs have garnered significant research interest regarding the effect of disorder on the electronic (3–5), thermal (6, 7), structural (8–10), and mechanical properties (11). However, it is the novel synthetic protocol by Tian *et al.* that turned AMCs into a class of amorphous materials resolved along a well characterized morphological axis (12).

Our focus here is on electrical conductance in AMCs, a property which was shown to have remarkable sensitivity to morphology. It was reported that a small change in synthetic conditions of AMC films led to a dramatic billion-fold increase in the sheet conductance (12). Building a mathematical relationship between morphology and conductance is a way to gain insight into this instability. From the computational perspective, however, modeling charge transport in such systems is extremely challenging because precise atomistic AMC structures need to be analyzed at the mesoscale, the scale of experimental measurements. Since the AMC is a covalently-bonded network of conjugated carbons and cannot be meaningfully fragmented, a good model must generate and analyze high quality atomistically resolved mesoscale samples. By anchoring computational results in the nuanced and rich experimental data from AMC experiments, in this paper, we aim to put to work the novel machine-

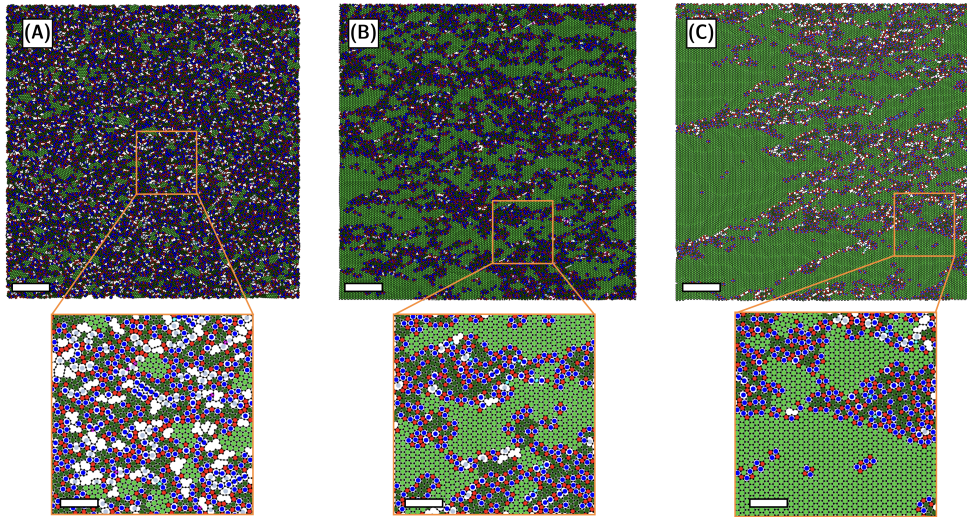


Figure 1: MAP-generated AMCs. To highlight the topological composition of AMC samples, pentagons are highlighted in red, isolated hexagons are in dark green, crystalline hexagons are in lime green (see Section 2 of Methods (13) for a technical definition of isolated and crystalline hexagons), 7- and 8-membered rings are in dark blue, 9- and 10-membered rings are in grey, squares are in turquoise, and triangles are in pink. **(A)** Example structure from the sAMC-500 ensemble. **(B)** Example structure from the sAMC-q400 ensemble. **(C)** Example structure from the sAMC-300 ensemble. *Scale bars:* 5 nm for the main figures, and 1.5 nm for the insets, which correspond to magnified regions of the full structures.

learning-augmented simulation methodologies (14–16), unravel the morphology-conductance relationship in AMCs, and demonstrate that computational modeling can be a helpful tool in amorphous materials research.

Computational generation of morphologically distinct AMC ensembles

For the purposes of our analysis we generate three ensembles of morphologically-distinct mesoscale AMCs: two to be compared directly with experimentally reported data, and one to be used to demonstrate an ambiguity in the currently accepted AMC morphology classification method. Samples of the three morphological classes are shown in Figure 1. Each mesoscopic AMC has the dimensions of roughly $40 \text{ nm} \times 40 \text{ nm}$ and was generated using a sampling approach based on generative machine learning: the Morphological Autoregressive Protocol (MAP) (14, 15). This approach takes advantage of decaying structural correlations characteristic of amorphous materials to sample large-scale conformations by extrapolating from smaller (order of correlation length) samples. The training samples in this work were produced by a Monte-Carlo bond switching protocol driven by ML energies from the C-GAP-17 potential (16). In order to reduce the error bars on computational predictions to acceptable levels more than 200 samples were generated in each ensemble. For full technical details on dataset generation and the MAP implementation, see Section S1 of Methods (13).

To classify the morphology we use the same descriptors as Tian *et al.*: (i) the pair correlation function $g(r)$ averaged over each ensemble (see Figure 2A); (ii) the short- and medium-range order parameters, ρ_{sites} and $\log \eta_{\text{MRO}}$ defined below, (iii) the distribution of different types of carbon rings, and (iv) the area distribution of crystalline inclusions. The order parameter ρ_{sites} is the number of connected clusters of undistorted carbon atoms per unit area in a given structure. A carbon atom is considered undistorted if the bond lengths and bond angles it forms with its immediate neighbours deviate by under 10% from those in pristine graphene. This order parameter therefore measures the persistence of short-range order in a AMC sample. The medium-range order parameter $\log \eta_{\text{MRO}}$ order parameter is related to the integral of the pair correlation function in the medium range distance between 4 \AA and

12 Å. For technical details on all four descriptors see Section S2 of Methods (13).

We start morphology analysis with the most disordered ensemble, see Figure 1A for sample visualization and the green line in Figure 2A for evidence of fast-decaying pair correlations. As shown in Figure 2B, the green set of points corresponding to this ensemble, it is positioned in the upper left corner of the $\log \eta_{\text{MRO}}$ vs. ρ_{sites} plot – close to the position of AMC-500 ensemble reported by Tian *et al.* (12), and its distribution of rings shown Figure 2C (in green) is close to the experimental AMC-500 ensemble as well. Due to its similarity in morphological metrics to the AMC-500 from reference (12), we will refer to it as “simulated AMC-500” or sAMC-500 henceforth.

The next ensemble we discuss is the most graphene-like ensemble shown in Figure 1C. It is much more ordered as it contains large sections of almost perfect hexagonal order (graphene-like hexagonal motifs are highlighted in lime green in Figures 1A-C). This ensemble displays ring statistics that are close to the AMC-300 samples in Tian *et al.* (12) and it is found in a similar region of the $\log \eta_{\text{MRO}}$ vs. ρ_{sites} space. We will, therefore, refer to this ensemble as “simulated AMC-300” or sAMC-300.

The third ensemble, visualized in Figure 1B, is somewhat difficult to classify. Similarly to Tian *et al.*’s AMC-400, our third set of structures exhibits a degree-of-disorder greater than that of the sAMC-300 samples, but lower than that of those in the sAMC-500 as inferred from observations of disorder in Figures 1A-C, and the intermediate decay of correlations in Figure 2A. It is found in a position similar to AMC-400 in $(\log \eta_{\text{MRO}}, \rho_{\text{sites}})$ space. However, the ring statistics (Figure 2C in purple) show a balance of crystalline hexagons (6-c) vs. non-crystalline hexagons (6-i) that is reversed with respect to the experimentally generated AMC-400 samples (see Figure 2h in reference (12)) - namely in simulated samples the crystalline hexagons 6-c are much more common than non-crystalline 6-i hexagons, while in experiments the opposite is true. Because of this mismatch, we will refer to this simulated ensemble as sAMC-q400 (for “quasi-400”). This ensemble highlights the possibility of non-unique classification of morphologies based on position in the $(\log \eta_{\text{MRO}}, \rho_{\text{sites}})$ space.

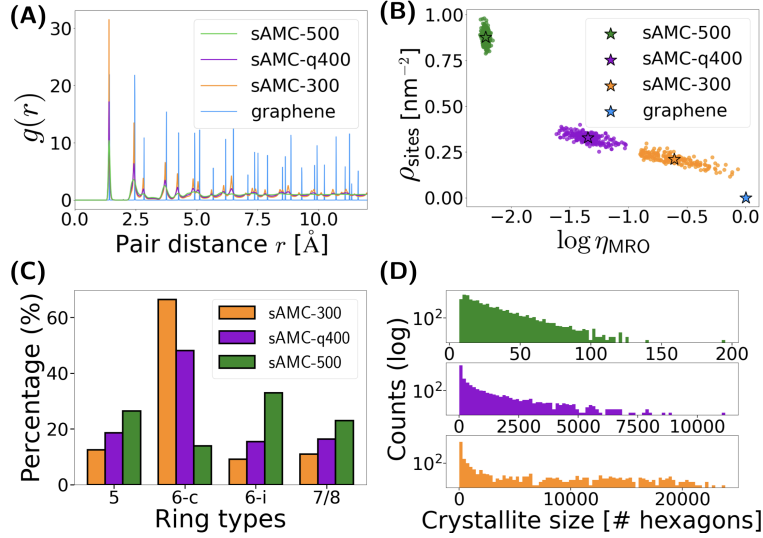


Figure 2: Characterisation of disorder in AMC. (A) Ensemble-averaged pair correlation functions of sAMC-500 (green), sAMC-q400 (purple), and sAMC-300 (orange). The pair correlation function $g(r)$ of pristine graphene (blue) is also shown as a reference. (B) Scatter plot of all the structures in the three ensembles in $(\log \eta_{\text{MRO}}, \rho_{\text{sites}})$ space. The green, purple, and orange stars mark the respective positions of the sAMC-500, sAMC-q400, and sAMC-300 ensemble averages. The position of a 40 nm \times 40 nm graphene flake is shown as a blue star for reference. In this space sAMC-300 is closer to graphene than to the highly disordered sAMC-500. (C) Carbon ring size distributions in generated AMC ensembles. Crystalline and isolated hexagons are respectively denoted 6-c and 6-i. (D) Distribution of crystallite (i.e. cluster of crystalline hexagons) areas in sAMC-500 (top, green), sAMC-q400 (middle, purple), and sAMC-300 (bottom, orange) structures.

Conductance prediction from percolation theory

It is widely accepted that the lack of periodicity in amorphous materials leads to spatially localized electronic states (17–19). This phenomenon prevents charge carriers from travelling coherently across the material. Instead, charge transport in amorphous phases is modelled within a variable range hopping (VRH) picture, wherein charge carriers incoherently travel between localised sites by exchanging energy with a bath of molecular vibrations (20). While the billionfold enhancement in conductance displayed by the high-crystallinity AMC samples in reference (12) might lead one to suspect that a coherent band transport mechanism may dominate, two experimental observations suggest that the VRH picture remains valid even for such ordered AMCs. Firstly, their resistance-temperature relation obeys the two-dimensional Mott law (2, 12, 20), which is typical of VRH in systems with a slowly varying density of states (DOS) (20–22). Secondly, the largest crystalline domains in the most ordered AMC samples are reported to extend up to 3.5 nm – three orders of magnitude shorter than the length of the samples typically used to perform the resistance measurements (2, 12). Charge carriers must therefore travel across disordered regions of the film, removing the possibility of crystalline band transport, and making the existence of long-lived mesoscale delocalised states unlikely.

The hopping sites in the VRH picture are usually taken to be spatially localised eigenstates of the electronic hamiltonian (22). Since AMCs are sp^2 -hybridized conjugated carbon systems (2), it may be safely assumed that only the π -network electrons contribute to conduction. We therefore model the electronic structure of mesoscopic AMC fragments using an all-atom tight-binding hamiltonian $\mathcal{H} = \sum_{\langle i,j \rangle} t_{ij}(|\varphi_i\rangle\langle\varphi_j| + |\varphi_j\rangle\langle\varphi_i|)$, where $|\varphi_i\rangle$ denotes the $2p_z$ orbital centered on the i th carbon in the AMC sample. The sum is carried out over all nearest-neighbour pairs $\langle i,j \rangle$, and the semi-empirical parametrisation of the hopping elements t_{ij} is adapted from prior works (23, 24), see Section S3 of Methods (13) for details.

We work with 40 nm \times 40 nm atomistically resolved samples, and thus do not resort to coarse-graining, applying periodic boundary conditions, modeling only partially resolved structures, or any other kind of commonly employed simplifications. While the enormous size of the hamiltonian matrices and the large number of samples in our ensembles preclude

us from resolving the full eigenspectrum using standard numerical routines, doing so is not necessary for this problem. Since thermally activated conductance is expected to be mediated by a relatively narrow band of thermally accessible states, we partially diagonalise each hamiltonian using the Lanczos algorithm (25), which is well-suited to the tight-binding hamiltonians' sparse structure (Section S4 of Methods (13)). We thereby obtain the subset of molecular orbitals (MOs) whose energies lie within $4k_B T$ above the chemical potential μ at room temperature ($T = 300$ K), under different gating conditions. We focus on three regimes: (i) the ungated regime in which $\mu = \epsilon_F$, the sample's Fermi level at half-filling; (ii) the regime where a strong negative gate voltage is applied and $\mu = \epsilon_0$, the smallest eigenvalue of \mathcal{H} ; and (iii) the regime where a strong positive gate voltage is applied and $\mu = \epsilon_N - 4k_B T$ where ϵ_N is the greatest eigenvalue of \mathcal{H} .

It is expected that solutions obtained from such low level of theory may possess some degree of artifacts. In this case, we noticed that some of the eigenstates we obtain are delocalised in ways that we do not expect to withstand the effects of decoherence and localization due to factors that were not included in our calculation but are certainly present in the real system. Some of the factors that are not included in our model are the electron-electron and electron-phonon interactions, as well as the interactions with substrate and distortions such as ripples or buckling that AMC sheets are expected to undergo at ambient conditions (26,27), which would disrupt the extent of sp^2 conjugation and contribute to electronic localisation (28). In our case, the delocalized eigenstates/molecular orbitals (MOs) which we regarded as pathological typically has several disjoint pockets of high electronic density separated by distances that can span 10's of nm, almost the entire AMC structure's length (see Fig. S1 in Methods (13)). This behavior was more common among MOs found near ϵ_F , whereas the eigenstates at the band edges expectedly tended to be localised, with very few exceptions. In order to model VRH of charges we have made the choice to construct conduction space in which we artificially localize the pathological MOs into multiple disjoint charge-hopping sites.

To construct the state space for the VRH network, we have developed a procedure based on k -means clustering to extract hopping sites from the MOs supported by each AMC fragment, (see Section S5 of Methods (13)). This approach partitions each (n^{th}) MO $|\psi_n\rangle$

into a set of m_n localised states $\{|s_{n,i}\rangle\}_{i=1,\dots,m_n}$, from which site positions $\{\mathbf{R}_{n,i}\}_{i=1,\dots,m_n}$ and delocalisation radii $\{a_{n,i}\}_{i=1,\dots,m_n}$ can be extracted. MOs that are already localised are left unchanged by this procedure. As the last correction mechanism for numerical artifacts in the electronic structure modeling, the occasional sites whose effective area $\pi a_{n,i}^2$ exceeded the area of the largest crystalline inclusion found in the ensemble (Fig. 2D) were considered numerically artificial and removed from our calculation. We tabulate the maximum allowed site radii a_{max} for the three AMC ensembles in Table 1.

Having constructed the VRH space, we apply percolation theory to estimate AMC conductances. Percolation theory has been very successfully applied as an analytical framework to estimate the VRH conductance of various classes of disordered semiconductors whose density of states (DOS) has a simple closed-form expression (e.g. a Gaussian distribution) (21, 29–37). Practically, percolation-based approaches are attractive because they do not suffer from stability or convergence issues associated with the usual techniques of VRH simulations like the solution of a transport master equation (38, 39), or Monte Carlo sampling of hopping trajectories (40, 41). Seeing as the DOS profiles for the three morphological classes we consider are not known analytically, we developed a numerical implementation of percolation of theory, which yields an ensemble-averaged estimate for charge conductance.

We define the hopping rate ω_{ij} between sites i and j using a Miller-Abrahams expression which we modified to accommodate for variable site radii: $\omega_{ij} \sim e^{-\xi_{ij}}$, where the dimensionless quantity ξ_{ij} can be thought of as an effective distance between sites i and j and depends on the sites' positions, energies, and radii (see Eqn. S5 in Methods (13) for ω_{ij}). Each structure admits a critical distance ξ_c at which a cluster of sites obeying $\xi_{ij} \leq \xi_c$ percolates the sample by connecting its right edge to its left edge. The randomness inherent to the AMC fragments, as well as their finite size, will lead ξ_c to fluctuate from fragment to fragment. Following an approach similar to Rodin and Fogler (36), we estimate each ensemble's conductance σ as follows:

$$G = \frac{q_e^2 \omega_0}{k_B T} \int d\xi e^{-\xi} P(\xi),$$

where $P(\xi)$ is the probability of having a percolating cluster through sites obeying $\xi_{ij} \leq \xi$ in a given ensemble, $\omega_0 = 1 \text{ fs}^{-1}$ is the escape frequency, q_e is the elementary charge, k_B is

Boltzmann’s constant, and $T = 300$ K denotes temperature. See Section S6 of Methods (13) for technical details.

Results and Discussion

Next, we summarize and discuss the results of our modeling. First we reproduce experimentally observed conductances reported in Ref. (12) for sAMC-500 and sAMC-300 ensembles. Then we discuss the deviation of the predicted conductance for the sAMC-q400 ensemble relative to the experimentally characterized in Ref. (12) AMC-400. Our results imply that a unique map between the $(\log \eta_{\text{MRO}}, \rho_{\text{sites}})$ space and conductance, in contradiction to previous assertions (e.g., Figure 4a in Ref. (12)), does not exist. We conclude with the discussion of the possibility of controlling conductance in AMCs by applying gate voltage and in effect modifying the characteristics of the charge transport pathways while keeping the AMC sample unchanged.

Conductance

We performed our conductance calculations at $T = 300$ K, under different gating conditions. The results are plotted in Figure 3A, and a summary is tabulated in Table 1. First, we focus on the conductance in the ungated case in which charge transport is carried by states close to the Fermi energy (ϵ_F) of the AMC, the middle set of data-points in Figure 3A. The two ensembles that we may directly compare to experimental data are sAMC-300 shown in orange and sAMC-500 shown in green. We observe a conductance gap of 5 orders of magnitude between the two in our calculations which matches well the gap observed in Ref. (12), see Figure 3d there.

Of particular interest is the high conductance of the sAMC-q400 ensemble which is found to be on par with the high, relative to other AMCs, conductance of sAMC-300. The sAMC-q400 ensemble falls close to the experimental AMC-400 ensemble in the $(\log \eta_{\text{MRO}}, \rho_{\text{sites}})$ space with the center close to $(-1.3, 0.3)$ point compared to approximately $(-1.25, 0.35)$ in the experimental case. However, AMC-400 was experimentally and theoretically shown to be a perfect insulator. Previous modeling approaches assigned a smooth map from the

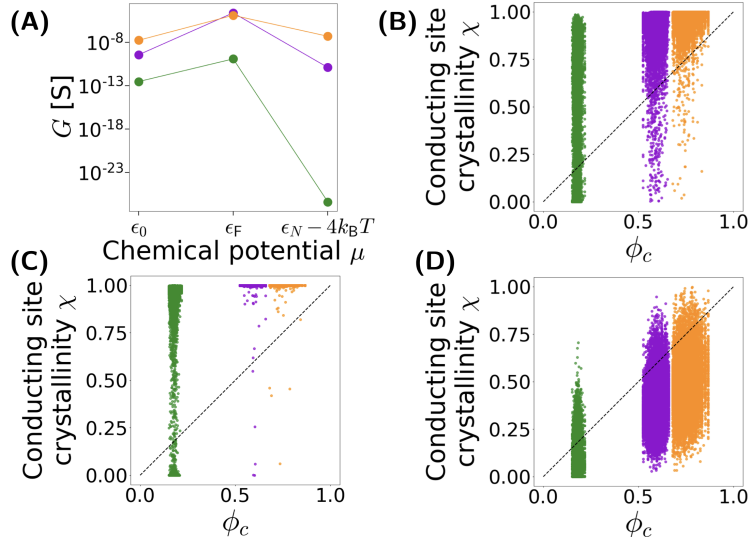


Figure 3: Electronic conductance and the morphology of conducting pathways in AMC. (A) Electrical conductance G of the three sAMC ensembles, at different gate voltages. The error bars are omitted because they are too small to be visible (see Table 1). (B)-(D) Crystallinity χ of the electron hopping sites in a conduction network, plotted against the fraction of crystalline atoms ϕ_c in the AMC samples under the three gating regimes: (B) $\mu = \epsilon_0$ – the smallest eigenvalue of electronic Hamiltonian, (C) $\mu = \epsilon_N - 4k_B T$ – where ϵ_N is the largest eigenvalue of electronic Hamiltonian, and (D) $\mu = \epsilon_F$. Sites from sAMC-500 samples are shown in green, sites from sAMC-q400 samples are in purple, and sites from sAMC-300 samples are in orange. Sites that are clustered high above the diagonal are localized on crystalline regions while those those clustered under the diagonal show preference for defects.

$(\log \eta_{\text{MRO}}, \rho_{\text{sites}})$ space to conductance with vanishing values in this particular region of the $(\log \eta_{\text{MRO}}, \rho_{\text{sites}})$ space and they would struggle to reconcile the sharp difference between the behaviors of AMC-400 and sAMC-q400. Our contrarian result demonstrates that the morphology-conductance relationship in AMC is more complex than previously thought. The morphological difference between sAMC-q400 and AMC-400 is visible in ring-distribution statistics (Figure 2C).

Structural metamorphosis of current-carrying regions through gating

Finally, we discuss the possibility to weakly decouple the conductance from morphology in AMCs. The idea behind this is that molecular orbitals in different regions of the spectrum tend to have differing morphological characteristics. We previously discussed the emergence of edge-states around the middle of the spectrum and bulk-localization of MOs towards the edges of the 'band' in amorphous graphene nanoflakes (42). Similar behavior is observed in mesoscale samples of AMCs as well, and by applying gate voltage we, in effect, modify morphological characteristics of the conducting VRH networks while keeping the overall atomistic morphology fixed.

We note that the effects of applying a gate voltage in our simplified modeling reflect only the characteristics of the MOs that carry the current under the different conditions - the changes to resistance of contacts for example are neglected. Under this idealized assumption we observe that conductance depends rather strongly on gating and that more disordered AMCs show larger sensitivity. To understand the origin of this effect we need to quantify the morphological changes, i.e., the structural metamorphosis, that conducting networks undergo when a gate voltage is applied.

The connection between the morphology and conductance can be further clarified by examining the morphologies of only those regions of AMC samples on which the electronic states that dominate charge transport are localized. To do so we define the crystallinity χ of a given VRH state $|\psi\rangle$ as follows:

$$\chi(|\psi\rangle) = \sum_{j \in \mathcal{C}} |\langle \varphi_j | \psi \rangle|^2, \quad (1)$$

where \mathcal{C} corresponds to the set of crystalline atoms – i.e. atoms belonging to a crystalline

	sAMC-500	sAMC-q400	sAMC-300
a_{max} [Å]	18.03	136.47	199.33
p_{6c} [%]	13.64	48.11	66.41
$G(\mu = \epsilon_0)$ [S]	$(2.99 \pm 2.43) \cdot 10^{-13}$	$(3.64 \pm 1.60) \cdot 10^{-10}$	$(1.72 \pm 1.20) \cdot 10^{-8}$
$G(\mu = \epsilon_F)$ [S]	$(1.24 \pm 0.11) \cdot 10^{-10}$	$(2.51 \pm 0.40) \cdot 10^{-5}$	$(1.30 \pm 0.15) \cdot 10^{-5}$
$G(\mu = \epsilon_N - 4k_B T)$ [S]	$(4.11 \pm 4.03) \cdot 10^{-27}$	$(1.27 \pm 1.26) \cdot 10^{-11}$	$(5.00 \pm 3.32) \cdot 10^{-8}$

Table 1: Summary of transport properties and structural characteristics exhibited by the simulated AMC ensembles studied in this work. For each ensemble, a_{max} is the effective radius of the largest crystalline inclusion (Fig. 2 D) and the delocalisation radius cutoff used in the percolation calculation; p_{6-c} is the percentage of crystalline hexagons (based on Fig. 2 C); and $G(\mu = E)$ denotes conductance when gating sets each structure’s chemical potential μ to energy E .

hexagon (previously referred to as 6-c). In words, $\chi(|\psi\rangle)$ corresponds to the aggregated density of $|\psi\rangle$ which lies on the crystalline regions of a given AMC sample.

In Figures 3B-D, we plot the crystallinity of each VRH site belonging to a percolating cluster against the fraction of crystalline atoms ϕ_c in the relevant AMC sample. Focusing first on the gated regimes summarized in 3B and C, we find that conducting sites at the band edges (i.e. far from ϵ_F), tend to be localized preferentially on crystalline inclusions since they tend to lie above the diagonal and thereby satisfy $\chi > \phi_c$, meaning that they are more crystalline than the rest of the structure. We infer from this that charge transport in these regimes is mostly carried by hopping from one crystalline site to another, giving a partial rationalization to an intuitive and common modeling assumption.

The picture changes when we move to the ungated case shown in Figures 3D. There we find that unlike the states at the band’s edges, the mid-spectrum eigenstates produce VRH sites which predominantly satisfy $\chi < \phi_c$ (Fig. 3D), i.e., that are preferentially found on defects in all three ensembles. Charge hopping in the ungated regime therefore takes place predominantly over the disordered regions of AMC. Within the framework of VRH, the bias of the conduction networks towards disordered regions puts the propensity of defects in competition with the localization of the electronic states. The interplay between these two

properties gives rise to the predicted conduction trends, and originates in the dependence of the inter-site hopping rates ω_{ij} on the sites' radii and site-site distances (Eqn. S5 in Methods (13)). For instance, our calculations show that sAMC-q400 exhibits ungated conductance close to sMAC-300 in spite of being much more disordered overall. This happens because it strikes a balance between the two competing effects: it contains more extensive disordered regions to increase the density of hopping sites relative to sAMC-300, while also retaining enough structural order to give rise to sites with reasonably large radii.

Under our simplifying assumptions, the gate-voltage modulation charge transport in AMCs is owed to the metamorphosis of the conducting states along the electronic energy spectrum. This ready and reversible tunability of AMC's conductance – taken together with the low heat conductance which is owed to its inherently disordered bonding network (7) – make is potentially an attractive candidate for thermoelectric applications. This observation is likely to remain at the conceptual level until effective strategies are invented to increase conductivities in AMCs to levels sought after in thermoelectric materials, i.e. $\sim 10 \text{ S cm}^{-1}$ (43). In the past, nitrogen doping has been shown enhance the electrical conductance of AMC by an order of magnitude (44) and sets a precedent for future developments in this space.

Conclusion

In this work we have combined deep learning-enhanced simulation techniques with percolation theory to model charge conductances in three morphologically distinct mesoscale AMCs. We have overcome the challenges of modeling electronic conductance in mesoscale atomistically resolved covalently bonded networks of conjugated carbons by developing a custom partial diagonalisation procedure based on the Lanczos algorithm and adapted the percolation theory calculation of charge conductance to the peculiarities of the AMC system. Our protocol is noteworthy in that it avoids the artifacts that may arise from applying periodic boundary conditions to aperiodic amorphous structures (a common practice), or from oversimplifying assumptions regarding transport mechanism. We reproduce the reported dependence of charge conductance on morphology and discuss the ambiguous relationship between incomplete/partial measures of morphology and conductance. By conducting a crystallinity analysis of the conducting sites we show that they metamorphose in response to gate voltage

from being localized on crystallites at band edges to being localized on defects around the Fermi energy. Inspired by this observation, we explore the possibility to decouple the AMC morphology from electronic conductance by applying a gate voltage and comment on the potential of thermoelectric tunability in amorphous conductors.

References and Notes

1. A. Madanchi, *et al.*, Is the Future of Materials Amorphous? Challenges and Opportunities in Simulations of Amorphous Materials (2024), <https://arxiv.org/abs/2410.05035>.
2. C.-T. Toh, *et al.*, Synthesis and properties of free-standing monolayer amorphous carbon. *Nature* **577** (7789), 199–203 (2020).
3. V. Kapko, D. Drabold, M. Thorpe, Electronic structure of a realistic model of amorphous graphene. *physica status solidi (b)* **247** (5), 1197–1200 (2010).
4. D. Van Tuan, *et al.*, Insulating behavior of an amorphous graphene membrane. *Physical Review B* **86** (12), 121408 (2012).
5. A. Lherbier, *et al.*, Highly defective graphene: A key prototype of two-dimensional Anderson insulators. *Nano Research* **6**, 326–334 (2013).
6. T. Zhu, E. Ertekin, Phonons, localization, and thermal conductivity of diamond nanowires and amorphous graphene. *Nano letters* **16** (8), 4763–4772 (2016).
7. A. Antidormi, L. Colombo, S. Roche, Thermal transport in amorphous graphene with varying structural quality. *2D Materials* **8** (1), 015028 (2020).
8. A. Kumar, M. Wilson, M. Thorpe, Amorphous graphene: a realization of Zachariasen’s glass. *Journal of Physics: Condensed Matter* **24** (48), 485003 (2012).
9. Y.-T. Zhang, *et al.*, Structure of amorphous two-dimensional materials: elemental monolayer amorphous carbon versus binary monolayer amorphous boron nitride. *Nano Letters* **22** (19), 8018–8024 (2022).
10. D. Chen, *et al.*, Stone–wales defects preserve hyperuniformity in amorphous two-dimensional networks. *Proceedings of the National Academy of Sciences* **118** (3), e2016862118 (2021).

11. L. C. Felix, R. M. Tromer, P. A. Autreto, L. A. Ribeiro Junior, D. S. Galvao, On the mechanical properties and thermal stability of a recently synthesized monolayer amorphous carbon. *The Journal of Physical Chemistry C* **124** (27), 14855–14860 (2020).
12. H. Tian, *et al.*, Disorder-tuned conductivity in amorphous monolayer carbon. *Nature* **615** (7950), 56–61 (2023).
13. Methods are available as supplementary material.
14. M. Kilgour, N. Gastellu, D. Y. Hui, Y. Bengio, L. Simine, Generating multiscale amorphous molecular structures using deep learning: a study in 2D. *The Journal of Physical Chemistry Letters* **11** (20), 8532–8537 (2020).
15. A. Madanchi, M. Kilgour, F. Zysk, T. D. Kühne, L. Simine, Simulations of disordered matter in 3D with the morphological autoregressive protocol (MAP) and convolutional neural networks. *The Journal of Chemical Physics* **160** (2) (2024).
16. V. L. Deringer, G. Csányi, Machine learning based interatomic potential for amorphous carbon. *Physical Review B* **95** (9), 094203 (2017).
17. P. W. Anderson, Absence of diffusion in certain random lattices. *Physical review* **109** (5), 1492 (1958).
18. D. J. Thouless, Electrons in disordered systems and the theory of localization. *Physics Reports* **13** (3), 93–142 (1974).
19. P. A. Lee, T. V. Ramakrishnan, Disordered electronic systems. *Reviews of modern physics* **57** (2), 287 (1985).
20. N. F. Mott, E. A. Davis, *Electronic processes in non-crystalline materials*, vol. 14 (Oxford University Press Oxford) (1971).
21. V. Ambegaokar, B. Halperin, J. Langer, Hopping conductivity in disordered systems. *Physical review B* **4** (8), 2612 (1971).
22. B. I. Shklovskii, A. L. Efros, *Electronic properties of doped semiconductors*, vol. 45 (Springer Science & Business Media) (1984).

23. F. Sterpone, P. J. Rossky, Molecular modeling and simulation of conjugated polymer oligomers: Ground and excited state chain dynamics of PPV in the gas phase. *The Journal of Physical Chemistry B* **112** (16), 4983–4993 (2008).
24. A. E. Jailaubekov, *et al.*, Hot charge-transfer excitons set the time limit for charge separation at donor/acceptor interfaces in organic photovoltaics. *Nature materials* **12** (1), 66–73 (2013).
25. G. H. Golub, C. F. Van Loan, *Matrix Computations* (JHU press), 3rd ed. (1996).
26. J. C. Meyer, *et al.*, The structure of suspended graphene sheets. *Nature* **446** (7131), 60–63 (2007).
27. J. Ma, D. Alfè, A. Michaelides, E. Wang, Stone-Wales defects in graphene and other planar sp²-bonded materials. *Physical Review B—Condensed Matter and Materials Physics* **80** (3), 033407 (2009).
28. S. Krasavin, V. Osipov, Electrical resistivity of polycrystalline graphene: Effect of grain-boundary-induced strain fields. *Scientific Reports* **12** (1), 14553 (2022).
29. B. Shklovskii, A. Efros, Impurity band and conductivity of compensated semiconductors. *Soviet physics JETP* **33** (2) (1971).
30. G. Pike, C. Seager, Percolation and conductivity: A computer study. I. *Physical review B* **10** (4), 1421 (1974).
31. M. Grünewald, P. Thomas, A hopping model for activated charge transport in amorphous silicon. *physica status solidi (b)* **94** (1), 125–133 (1979).
32. M. Vissenberg, M. Matters, Theory of the field-effect mobility in amorphous organic transistors. *Physical Review B* **57** (20), 12964 (1998).
33. S. Baranovskii, I. Zvyagin, H. Cordes, S. Yamasaki, P. Thomas, Percolation approach to hopping transport in organic disordered solids. *physica status solidi (b)* **230** (1), 281–288 (2002).

34. O. Rubel, S. Baranovskii, P. Thomas, S. Yamasaki, Concentration dependence of the hopping mobility in disordered organic solids. *Physical Review B* **69** (1), 014206 (2004).
35. I. Zvyagin, A percolation approach to the temperature and charge carrier concentration dependence of the hopping conductivity in organic materials. *physica status solidi c* **5** (3), 725–729 (2008).
36. A. Rodin, M. Fogler, Hopping transport in systems of finite thickness or length. *Physical Review B* **84** (12), 125447 (2011).
37. A. Nenashev, *et al.*, Advanced percolation solution for hopping conductivity. *Physical Review B* **87** (23), 235204 (2013).
38. Z. Yu, D. Smith, A. Saxena, R. Martin, A. Bishop, Molecular geometry fluctuations and field-dependent mobility in conjugated polymers. *Physical Review B* **63** (8), 085202 (2001).
39. W. Pasveer, P. Bobbert, H. Huinink, M. Michels, Scaling of current distributions in variable-range hopping transport on two- and three-dimensional lattices. *Physical Review B* **72** (17), 174204 (2005).
40. H. Bäessler, Charge transport in disordered organic photoconductors. A Monte Carlo simulation study. *Physica Status Solidi B (Basic Research);(Germany)* **175** (1) (1993).
41. J. T. Willson, W. Liu, D. Balzer, I. Kassal, Jumping kinetic Monte Carlo: Fast and accurate simulations of partially delocalized charge transport in organic semiconductors. *The Journal of Physical Chemistry Letters* **14** (15), 3757–3764 (2023).
42. N. Gastellu, M. Kilgour, L. Simine, Electronic conduction through monolayer amorphous carbon nanojunctions. *The Journal of Physical Chemistry Letters* **13** (1), 339–344 (2022).
43. J. Liu, *et al.*, N-type organic thermoelectrics: demonstration of ZT_j 0.3. *Nature communications* **11** (1), 5694 (2020).

44. J. Zhao, *et al.*, Synthesis of large-scale undoped and nitrogen-doped amorphous graphene on MgO substrate by chemical vapor deposition. *Journal of Materials Chemistry* **22** (37), 19679–19683 (2012).
45. N. Gastellu, ArpackMAC, ArpackMAC repository on GitHub, <https://github.com/ngastellu/ArpackMAC>.
46. N. Gastellu, PercolateMAC, percolate_mac repository on GitHub, https://github.com/ngastellu/percolate_mac.
47. N. Gastellu, DisorderAnalysisMAC, disorder_analysis_MAC repository on GitHub, https://github.com/ngastellu/disorder_analysis_MAC.
48. A. Madanchi, sAMC generation, sAMC_generation repository on GitHub, https://github.com/ngastellu/sAMC_generation.
49. A. Van den Oord, *et al.*, Conditional image generation with pixelcnn decoders. *Advances in neural information processing systems* **29** (2016).
50. A. Van Den Oord, N. Kalchbrenner, K. Kavukcuoglu, Pixel recurrent neural networks, in *International conference on machine learning* (PMLR) (2016), pp. 1747–1756.
51. Z. El-Machachi, M. Wilson, V. L. Deringer, Exploring the configurational space of amorphous graphene with machine-learned atomic energies. *Chemical Science* **13** (46), 13720–13731 (2022).
52. S. J. Stuart, A. B. Tutein, J. A. Harrison, A reactive potential for hydrocarbons with intermolecular interactions. *The Journal of chemical physics* **112** (14), 6472–6486 (2000).
53. S. Plimpton, Fast parallel algorithms for short-range molecular dynamics. *Journal of computational physics* **117** (1), 1–19 (1995).
54. A. P. Thompson, *et al.*, LAMMPS-a flexible simulation tool for particle-based materials modeling at the atomic, meso, and continuum scales. *Computer Physics Communications* **271**, 108171 (2022).

55. J. Linderberg, Consistency requirement in the Pariser-Parr-Pople model. *Chemical Physics Letters* **1** (2), 39–41 (1967).
56. T. Ericsson, A. Ruhe, The spectral transformation Lanczos method for the numerical solution of large sparse generalized symmetric eigenvalue problems. *Mathematics of Computation* **35** (152), 1251–1268 (1980).
57. N. J. Higham, *Functions of matrices: theory and computation* (SIAM) (2008).
58. S. Lloyd, Least squares quantization in PCM. *IEEE transactions on information theory* **28** (2), 129–137 (1982).
59. F. Pedregosa, *et al.*, Scikit-learn: Machine Learning in Python. *Journal of Machine Learning Research* **12**, 2825–2830 (2011).
60. A. Miller, E. Abrahams, Impurity conduction at low concentrations. *Physical Review* **120** (3), 745 (1960).

Acknowledgments

We thank Zakariya El-Machachi and Volker Deringer for sharing amorphous graphene dataset they published in Ref. (16). and Alessandro Troisi for helpful tips on convergence issues in charge conductance calculations.

Funding: Funding from NSERC Discovery Grant, IVADO, and AI4Design program of the National Research Council of Canada is gratefully acknowledged.

Author contributions: AM built and trained the MAP models used to generate the AMC structures. The work was conceptualised by LS and NG. NG developed and implemented methods to partially diagonalise the tight-binding hamiltonians, to perform the numerical percolation calculations, to carry out the structural analysis of the AMC samples generated by AM, and generated all of the figures. NG and LS wrote the manuscript.

Competing interests: There are no competing interests to declare.

Data and materials availability: The code used for to instantiate and partially diagonalise the tight-binding hamiltonians can be found in the repository listed as reference (45).

Our numerical percolation code may be found in the repository listed as reference (46).

The code used for the structural analysis of MAP-generated AMC samples can be found in the repository listed as reference (47). The XYZ coordinate files describing the AMC structures used in our study can be also be found in this repository. These XYZ files can be used as input for the tight-binding and percolation codes mentioned above.

The code used for the training and deployment of MAP used to generate our three AMC ensembles can be found in the repository listed as reference (48).

Supplementary materials

Methods

Figs. S1 and S2

Table S1

References (48-60)

Supplementary Materials for
Disentangling morphology and conductance in
amorphous graphene

Nicolas Gastellu, Ata Madanchi, Lena Simine*

*Corresponding author. Email: lena.simine@mcgill.ca

This PDF file includes:

Methods

Figures S1 and S2

Table S1

Methods

Section S1 Modeling AMCs with the morphological autoregressive protocol (MAP)

We implement the MAP using the PixelCNN architecture (49, 50), a deep generative convolutional neural network. Morphologically distinct ensembles used in our analysis were generated following slightly different protocols. For instance, the ensemble sAMC-500 was generated following the protocol reported in reference (14) precisely. The training of the MAP model and the generation of ensembles sAMC-300 and sAMC-q400 is detailed below. The relevant code may be found on GitHub (48). We note that lack of consistency in generation protocols is immaterial in the context of morphology-function analysis and modeling decisions were based on practical considerations.

The MAP-PixelCNN model was trained on AMC samples ($2\text{ nm} \times 2\text{ nm}$) which were simulated by a Monte-Carlo bond switching protocol driven by ML energies from the C-GAP-17 potential (16) reported in Ref. (51). Three types of energies were used in the Monte-Carlo acceptance criterion: total energy, atomic energy of the defect pair and atomic energies of the defect pair and the topological nearest neighbours. This, in combination with different β values allowed sufficient sampling of disordered structures after 10,000 Monte-Carlo steps. In total, 13,944 200-atom fully sp^2 structures were obtained (just under 2.8 million atomic environments) using this framework with varying levels of disorder. For training the MAP ca. 800 structures were selected based on proportion of hexagon content (over 70%). To prepare the input, the training samples were discretised from real to grid space at a 0.2 \AA resolution, empty space was assigned the value 0, carbons were assigned the value 1.

Overall, the MAP learns the conditional probability distribution for the population of each grid point i given surrounding molecular context: $p(X_i|C_i)$, where the state X_i (carbon or empty space) depends on its local environment C_i . This environment, C_i , consists of all grid points within a 'receptive field' around i , capturing the short-to-medium range structural correlations inherent to AMC. To infer the conditional probability the model applies a softmax function to the final layer

$$p(X_i|C_i) = \text{softmax}(z_i, \tilde{T}) \tag{S1}$$

where z_i represents the logits predicted for grid point i being empty space or carbon and \tilde{T} is a hyperparameter. The training is done by the stochastic gradient descent to minimize the loss function:

$$L = - \sum_i \sum_{j=0,1} t_{i,j} \log p(X_i = j|C_i) \quad (\text{S2})$$

where $t_{i,j}$ is one-hot encoded value at grid point i of type j (empty or carbon), and $p(X_i|C_i)$ is the prediction made by Eqn.S1.

By construction, the MAP allows autoregressive generation and extrapolation of molecular structures grid point by grid point, based solely on prior generated molecular fragments. During the generation process, the softmax function is followed by multinomial sampling using the normalized grid point probabilities to predict the grid point value. Since in our training samples, the most common motifs are the hexagonal rings, we used the hyperparameter \tilde{T} to artificially control the generation of these more abundant motifs - lowering it reliably produced increasingly ordered (containing larger graphene-like crystalline domains) AMC structures. The sAMC-500 ensemble contains 300 samples, the sAMC-q400 ensemble contains 218 samples, and the sAMC-300 ensemble contains 217 samples.

All structures we lightly post-processed by energy minimization using the AIREBO semiempirical reactive forcefield (52). The relaxation was carried out using the LAMMPS molecular dynamics software package (53, 54), with leniently defined energy and force tolerance parameters (10^{-9} and 10^{-12} eV/Å, respectively).

Section S2 Morphological characterization

Calculating ρ_{sites}

Following Tian *et al.* (12), we define the short-range order parameter ρ_{sites} as the number of connected clusters of undistorted carbon atoms per unit area, in a given fragment. As in reference (12), a carbon atom is considered undistorted if it is bonded to exactly three neighbours and if the lengths and angles of the bonds connecting it to its neighbours deviate by less than 10% from the bond length/angle in a pristine graphene lattice ($r_{\text{CC}} = 1.42$ Å and $\theta = 2\pi/3$).

Using the adjacency matrix representation of each structure (see above section on obtain-

ing the carbon ring distributions of our sAMC structures), and depth-first search traversal of the graph it defines, we identify all clusters composed exclusively of undistorted carbons. We discard all clusters containing only a single carbon. We then divide the number n_c of such clusters by the sAMC structure’s surface area A , which we approximate as a rectangle: $A = L_x L_y$, where $L_x = \max_j x_j - \min_j x_j$ (idem for L_y). We thus have: $\rho_{\text{sites}} = n_c/A$.

Calculating η_{MRO}

The medium-range order (MRO) parameter η_{MRO} is defined as follows:

$$\eta_{\text{MRO}} = A_{\text{MRO}}(\text{AMC ensemble})/A_{\text{MRO}}(\text{graphene})$$

where A_{MRO} is derived from a given structure’s pair correlation function $g(r)$:

$$A_{\text{MRO}} = 2\pi \int_{r_1=4\text{\AA}}^{r_2=12\text{\AA}} |1 - g(r)|r \, dr .$$

We compute each sample’s pair correlation function by histogramming all interatomic distances smaller than $r_2 = 12 \text{ \AA}$. We use periodic boundary conditions (with the size of the cell chosen to be slightly bigger than the size of the structure at hand along x - and y -directions) when doing so to avoid artifacts associated with sampling the edges of the structure. Tian *et al.* used the pair correlation of a physical sample of graphene at room temperature to compute $A_{\text{MRO}}(\text{graphene})$ (12). Physical crystals at room temperature tend to have small local distortions (due to phonons), which broadens the otherwise delta function-like peaks in their pair correlation function (this is evident upon inspection of the graphene pair correlation function used by Tian *et al.* in their work – c.f. Figure 2 l-n of Ref. (12)). These broadened peaks will modify the $A_{\text{MRO}}(\text{graphene})$.

To be able to compare the values of η_{MRO} we obtain from our simulated structures to the η_{MRO} values by Tian *et al.*, we run a NVT molecular dynamics simulation of a graphene flake at $T = 300 \text{ K}$, using a timestep of 0.5 fs, and periodic boundary conditions. We ran the simulation for 100000 steps and used the structure at step 93000 (i.e. from a part of the simulation that was well-equilibrated) to compute the pair correlation from which we obtained $A_{\text{MRO}}(\text{graphene})$. We use the LAMMPS package to run the MD simulation.

Obtaining carbon ring distributions

To find the carbon cycles in a given sAMC structure, we build its graph representation by defining its adjacency matrix as follows:

$$M_{ij} = \begin{cases} 1 & \iff \text{atoms } i \text{ and } j \text{ are covalently bonded,} \\ 0 & \iff \text{otherwise.} \end{cases}$$

Here, we consider two atoms as covalently bonded if they are within 1.8 Å of each other.

We then form a list of all carbon triplets (i, j, k) such that carbons i and k are both bonded to carbon j (but not necessarily to each other). Each triplet then seeds a depth-first traversal of the structure’s graph, which identifies all of the cycles to which it belongs. We impose a ten-atom length cutoff on this depth-first search to keep our ring search computationally reasonable. Finally, we discard any cycle whose interior region contains one or more carbon atom which is not part of the cycle, using the ray-crossing algorithm. We then tally the number of carbons in each of the cycles obtained by our procedure to determine the ring distributions in our generated MAC samples.

Distinguishing crystalline and isolated hexagons

After having used our ring-finding method (described in the previous section) to identify the different rings in MAP-generated sAMC structures, we want to differentiate between the “crystalline” hexagons – which are clustered together into highly ordered, graphene-like regions – from the “isolated” hexagons, which tend to be more distorted than the crystalline ones, and are usually surrounded with carbon rings of different sizes. To do so, we begin by building a hexagon adjacency matrix M_h for structure, whose elements are defined as follows:

$$M_{h,ij} = \begin{cases} 1 & \text{if hexagons } i \text{ and } j \text{ share a vertex (i.e. a carbon atom),} \\ 0 & \text{if otherwise.} \end{cases}$$

We then use depth-first search of the structure’s hexagon graph (as defined by M_h) to find its connected components. We define a “flake” motif as a hexagon connected to six

Table S1: Tight-binding hamiltonian parameters

β_0 [eV]	μ_b [\AA^{-1}]	R_0 [\AA]	k_b [\AA^{-1}]
-2.438	2.035	1.397	0.405

other hexagons: we consider all seven hexagons as part of the flake. A crystalline hexagon is then defined as (i) part of a flake; or (ii) connected to a hexagon which is part of a flake. All hexagons which do not satisfy either of these two criteria are defined as isolated hexagons.

Section S3 Electronic structure: tight-binding hamiltonian

Starting from a AMC fragment with carbon atoms at positions $\{\mathbf{R}_i\}_{i=1,\dots,N}$, we dress each carbon with a $2p_z$ atomic orbital (AO) $|\varphi_i\rangle$. We then construct its tight-binding hamiltonian \mathcal{H} whose elements are defined using the Linderberg approximation (55):

$$\langle \varphi_i | \mathcal{H} | \varphi_j \rangle = t_{ij} = \begin{cases} \beta_0 e^{-\mu_b(R_{ij}-R_0)} (1 + k_b(R_{ij} - R_0)) & \iff 0 < R_{ij} = |\mathbf{R}_i - \mathbf{R}_j| \leq R_{\text{cutoff}}, \\ 0 & \iff R_{ij} > R_{\text{cutoff}}, \end{cases}$$

where β_0 , μ_b , and k_b are semi-empirical parameters describing sp^2 carbons, and R_0 is the equilibrium bond length between two carbon π -conjugated carbon atoms. The numerical values of these parameters can be found in Table S1. We set the nearest-neighbour cutoff distance $R_{\text{cutoff}} = 1.8 \text{\AA}$. The parametrisation of our tight-binding hamiltonian was adopted from previous publications (23, 24).

Section S4 Partial diagonalisation of tight-binding hamiltonians

Every AMC structure studied in this work contains $N \approx 60000$ carbon atoms. The hamiltonians we are working with are therefore massive matrices, whose diagonalisation using standard numerical techniques is completely intractable. However, each carbon atom typically has between two and four neighbours within R_{cutoff} , meaning that \mathcal{H} contains mostly null entries. We therefore represent each structure's hamiltonian as a sparse matrix to reduce the memory and time costs of its diagonalisation.

The full eigenspectrum of very large sparse matrices cannot be resolved with a single diagonalisation routine. Instead, specialised algorithms exist to obtain relatively small subsets of its eigenvector-eigenvalue pairs that occupy the extremal portions of its spectrum. The same algorithms can also find the eigenpairs that lie closest to (either above or below) some user-defined constant λ , using the shift-and-invert technique (56).

We use the Lanczos algorithm, as implemented in ARPACK library, to compute the different subsets of tight-binding eigenstates expected to be thermally accessible to charge hopping in the three gating regimes considered in this work. For the high positive (negative) gate voltage regime, we use the unshifted algorithm to obtain the 100 highest-energy (lowest-energy) eigenstates and keep only the eigenstates whose energies lie within $4k_B T$ of the maximum (minimum) energy, at $T = 300$ K.

For the ungated regime, we only consider the unoccupied eigenstates within $4k_B T$ of each sample's Fermi energy. To do so, we use the shift-inverted Lanczos algorithm with $\lambda = \epsilon_{\text{HOMO}}$, the energy of the highest occupied molecular orbital (HOMO), which we must estimate for each fragment. First, we use Gershgorin's circle theorem (57) to estimate the spectral range of \mathcal{H} :

$$\forall n \in \{1, \dots, N\}, \exists i \in \{1, \dots, N\}, |\epsilon_n - \mathcal{H}_{ii}| \leq \sum_{j=1}^N |t_{ij}| = r_i,$$

where ϵ_n denotes the n^{th} eigenvalue of \mathcal{H} , and t_{ij} are its off-diagonal elements. In words, the theorem states that any eigenvalue ϵ_n of \mathcal{H} lies within the range r_i of some diagonal element \mathcal{H}_{ii} .

Looping over all N rows (as indexed by i) in \mathcal{H} , we can obtain an interval $[E_{\min}; E_{\max}]$ which must contain all of its eigenvalues, where $E_{\min} = \min_i \{H_{ii} - r_i\}$ and $E_{\max} = \max_i \{H_{ii} + r_i\}$. We use this interval to produce an initial guess of the HOMO energy $\epsilon^{(0)} = (E_{\min} + E_{\max})/2$. Knowing that $\mathcal{H}_{ii} = 0$ for all i implies $E_{\min} = -E_{\max}$, which simplifies our initial guess $\epsilon^{(0)} = 0$ eV for all AMC structures.

Next, we perform a cheap LDLT factorisation:

$$\mathcal{H} - \epsilon^{(0)} = LDL^T$$

and count the number of negative entries of the diagonal matrix D to determine the number

$n_{<}^{(0)}$ of eigenvalues $\epsilon_i < \epsilon^{(0)}$. Our model of AMC’s electronic structure only accounts for a single electron per carbon atom and assumes spin degeneracy, so the HOMO energy will have exactly $N/2$ energies inferior or equal to it. We then define:

$$\delta^{(0)} = n_{<}^{(0)} - N/2,$$

and obtain a better estimate of ϵ_{HOMO} by running ARPACK’s Lanczos routine in eigenvalue-only mode (saves time and memory) with a low accuracy threshold ($\epsilon_{\text{tol}} = 10^{-5}$), and requiring $\delta^{(0)}$ eigenvalues.

We then loop over all approximate eigenvalues $\{\epsilon_i^{(1)}\}_{i=1, \dots, \delta^{(0)}}$ we obtain and estimate the number $n_{<,i}^{(1)}$ of true eigenvalues smaller than $\epsilon_i^{(1)}$, using the same LDL factorisation method as above. If one of our eigenvalue estimates $\epsilon_i^{(1)}$ satisfies $n_{<,i}^{(1)} = N/2$, we take it as our estimate ϵ_{HOMO} . Otherwise, we re-run the approximate diagonalisation of \mathcal{H} , until at some iteration n , we find a satisfactory eigenvalue estimate which satisfies $n_{<}^{(n)} = N/2$. We stress that the crude eigenvalue estimates we obtain at this point of our algorithm only serve to aim ARPACK’s diagonalisation routine to the correct region of each structure’s spectrum: we do not interpret them as useful physical quantities in our model.

Having obtained a rough estimate of ϵ_{HOMO} , we compute the number of Δ of energy eigenstates lie between ϵ_{HOMO} and $\epsilon_{\text{HOMO}} + 4k_{\text{B}}T$, with $T = 300$ K, using the LDLT factorisation of $\mathcal{H} - (\epsilon_{\text{HOMO}} + 4k_{\text{B}}T)$. We then run ARPACK’s Lanczos routine in eigenvalue-and-eigenvector mode with a tight convergence criterion ($\epsilon_{\text{tol}} = 10^{-8}$), $\lambda = \epsilon_{\text{HOMO}} - \delta\epsilon$, and ask for $\Delta + 1$ eigenpairs above λ . This finally yields between one and two hundred molecular orbitals $\{|\psi_{\text{HOMO}n}\rangle\}_{n=0, \dots, \Delta}$ and their associated energies $\{\epsilon_{\text{HOMO}+n}\}_{n=0, \dots, \Delta}$.

Finally we compute the Fermi energy as follows: $\epsilon_{\text{F}} = (\epsilon_{\text{HOMO}} + \epsilon_{\text{LUMO}})/2$, where $\epsilon_{\text{LUMO}} = \epsilon_{\text{HOMO}+1}$ is the second lowest energy (after ϵ_{HOMO}) obtained from this procedure. We do not use $|\psi_{\text{HOMO}}\rangle$ in our hopping calculations.

Section S5 Constructing the variable range hopping network sites

Procedure for localizing distributed molecular orbitals Here we describe the procedure for localizing the molecular orbitals (MOs) which were found to exhibit a torn morphology with multiple disjoint high-density pockets (see left panel of Fig. S1). For reasons

discussed in the main text, we extract hopping sites from a tight-binding molecular orbital (MO) $|\psi_n\rangle$ by partitioning the atoms in the sAMC sample using a k -means clustering approach. For each MO $|\psi_n\rangle$, we determine the number of clusters by estimating the number of high-electronic-density pockets it admits (more details in the following section), and proceed to group the atoms in the AMC sample using Lloyd’s algorithm (58, 59), weighed by its electronic density squared: $|\langle\varphi_j|\psi_n\rangle|^4$. Each cluster defines a new electronic state which is much more compactly localised than the original MO (see middle panel of Fig. S1). We take these states to be the hopping sites, and define their respective energies as the energies of their mother MO. For a given site $|s_i\rangle$, we define its position as:

$$\tilde{\mathbf{R}}_i = \frac{\sum_j \mathbf{r}_j |\langle\varphi_j|s_i\rangle|^4}{\sum_j |\langle\varphi_j|s_i\rangle|^4}, \quad (\text{S3})$$

where \mathbf{r}_j denotes the position of carbon atom j . We use the square of the site’s electronic density $|\langle\varphi_j|s_i\rangle|^4$ for the clustering of the sites and our evaluation of $\tilde{\mathbf{R}}_i$ to ensure that the hopping sites produced by this protocol are centered on or near a pocket of high electronic density.

We allow each structure to have sites with variable radii, which we define as:

$$a_i = \sqrt{\langle s_i | \mathbf{r}^2 | s_i \rangle - \langle s_i | \mathbf{r} | s_i \rangle^2}, \quad (\text{S4})$$

with \mathbf{r} denoting the position operator. The positions and radii of the sites obtained by this procedure are shown in the right panel of Figure S1.

Identifying the number of clusters

We define our hopping sites by running k -means clustering on the MOs we obtain from our partial diagonalisation routine. The number of clusters into which the algorithm partitions a given MO must be specified before running it. We define the number of clusters for each MO by using a crude estimate of the number of local maxima it exhibits.

For a given AMC fragment (for example see left panel in Fig. S2), our diagonalisation routine yields each eigenstate $|\psi_n\rangle$ as vectors in the basis of the carbon atoms’ $2p_z$ orbitals $\{|\varphi_j\rangle\}_{j=1,\dots,N}$:

$$|\psi_n\rangle = \sum_j M_{jn} |\varphi_j\rangle.$$

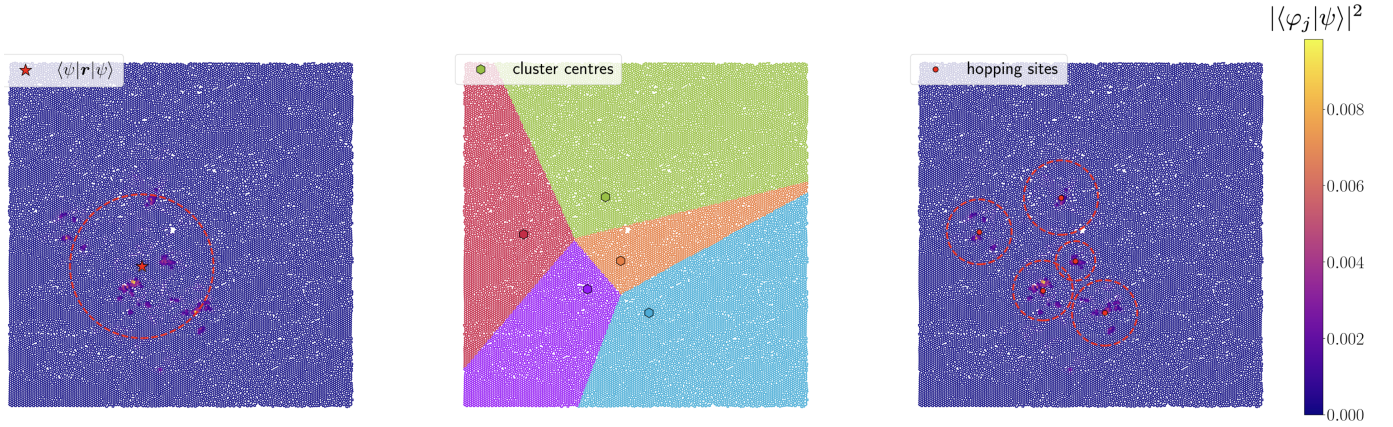


Figure S1: Procedure for obtaining the hopping sites. *Left:* Example of a molecular orbital (MO) $|\psi\rangle$ obtained by diagonalising the tight-binding hamiltonian \mathcal{H} . Atomic orbitals $|\varphi_j\rangle$ for whom $|\langle \varphi_j | \psi \rangle|^2 \geq 0.001$ are enlarged. The MO's center of mass $\langle \mathbf{r} \rangle$ is displayed as a star, and its radius of gyration $\sqrt{\langle \mathbf{r}^2 \rangle - \langle \mathbf{r} \rangle^2}$ is shown in red. *Middle:* Partition of the atoms in the AMC sample using our MO-weighted k-means clustering. The hexagons mark each cluster's center of mass. *Right:* Positions (dots) and radii (dotted circles) of the final hopping sites obtained from $|\psi\rangle$. The green cluster in **(B)** is devoid of any high electronic density pocket, so it does not yield a hopping site. The color bar applies to the left and right Figures and measures the electronic density. The dimensions of the samples are 40 nm \times 40 nm.

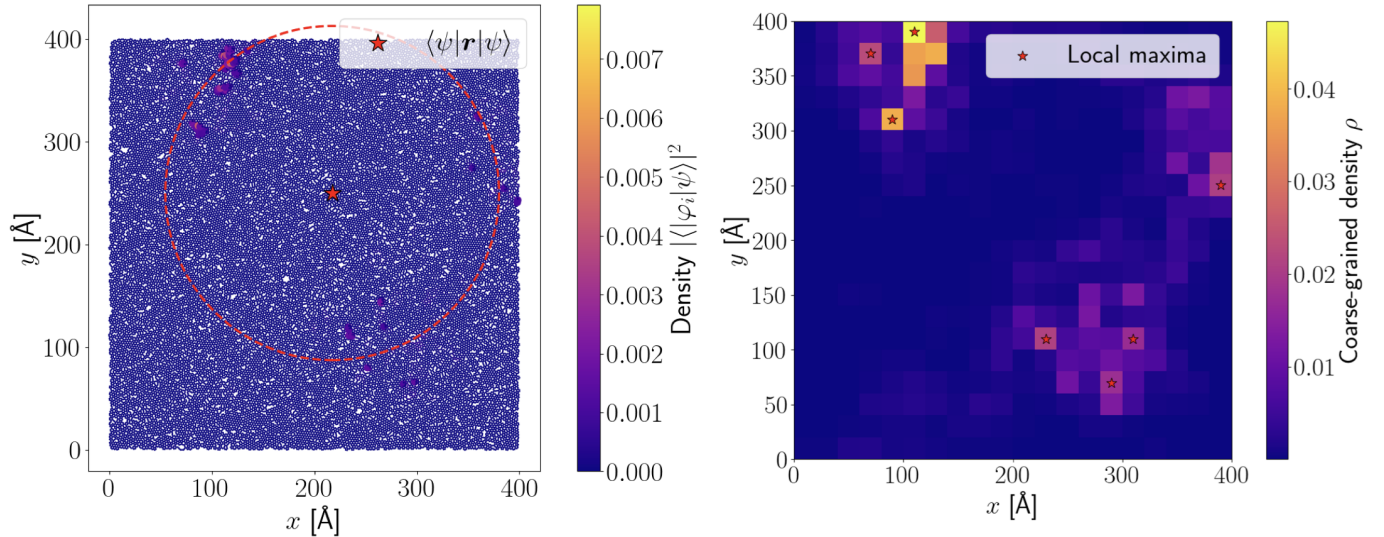


Figure S2: Procedure for obtaining the hopping sites. *Left:* Example of a molecular orbital (MO) $|\psi\rangle$ obtained by diagonalising the tight-binding hamiltonian \mathcal{H} . The red star represents the MO's average position $\langle \mathbf{r} \rangle = \langle \psi | \mathbf{r} | \psi \rangle$ and the red dotted circle centered on $\langle \mathbf{r} \rangle$ delimits the radius of gyration of $|\psi\rangle$ defined as: $R_g = \sqrt{\langle \psi | \mathbf{r}^2 | \psi \rangle - |\langle \mathbf{r} \rangle|^2}$. *Right:* Coarse-grained representation of $|\psi\rangle$ on a grid of 20×20 bins \mathcal{B}_{pq} . A coarser grid is used here for the sake of illustration. The bins corresponding to approximate local maxima are marked with a red star. In this example, the algorithm has identified 7 local maxima, so our k -means clustering protocol will partition $|\psi\rangle$ into at most 7 sites.

We project this representation back into real space by dividing the amorphous graphene into a grid of 100×100 bins $\{\mathcal{B}_{pq}\}_{p,q=1,\dots,100}$, and assigning to each bin \mathcal{B}_{pq} the coarse-grained electronic density value:

$$\rho(p, q) = \sum_{\mathbf{R}_j \in \mathcal{B}_{pq}} |\langle \varphi_j | \psi_n \rangle|^2.$$

We then identify the centers of the bins that locally maximise ρ (plotted in Figure S2, right panel) and obtain their real-space coordinates. To avoid over-partitioning our MOs, we ignore all bins \mathcal{B}_{pq} for which $\rho(p, q) < 0.3 \cdot \max_{p,q} \rho(p, q)$. We also impose a minimum distance of 20 Å between coarse-grained maxima we obtain using this procedure to avoid assigning multiple local maxima to a single high-density pocket.

Section S6 Numerical implementation of percolation theory

We describe hopping using a symmetric Miller-Abrahams² rate expression (60), adapted to accommodate sites with different radii:

$$\omega_{ij} = \omega_0 \exp \left\{ -f(|\mathbf{R}_i - \mathbf{R}_j|, a_i, a_j) - \frac{|\varepsilon_i - \mu| + |\varepsilon_j - \mu| + |\varepsilon_i - \varepsilon_j|}{2k_B T} \right\} = \omega_0 e^{-\xi_{ij}}, \quad (\text{S5})$$

where $\omega_0 = 10^{15} \text{ s}^{-1}$ is the attempt-to-escape frequency, i and j label the hopping sites, \mathbf{R}_i and \mathbf{R}_j denote their positions, a_i and a_j denote their radii, and $f(|\mu_1 - \mu_2|, a_1, a_2)$ corresponds to the overlap between two Gaussians with means μ_i , and standard deviations a_i :

$$f(|\mu_1 - \mu_2|, \sigma_1, \sigma_2) = \frac{\sigma_1 \sigma_2}{2\pi (\sigma_1^2 + \sigma_2^2)} \exp \left[-\frac{|\mu_1 - \mu_2|^2}{2(\sigma_1^2 + \sigma_2^2)} \right]. \quad (\text{S6})$$

To calculate the conductance G of an AMC ensemble, we must determine the percolation threshold ξ_c for each structure in the ensemble. For each structure, we iterate over its inter-site distances sorted in ascending order $\xi^{(1)} \leq \xi^{(2)} \leq \dots$, connecting all pairs of sites of (i, j) such that $\xi_{ij} \leq \xi^{(k)}$, on a given iteration step k . We halt the process once we have constructed a network of sites that connects a site strongly coupled to the left electrode, to a site strongly coupled to the right electrode. We then record the distance ξ_c at which a percolating cluster of sites emerges for that specific structure. We use the distribution of percolation thresholds we obtained for each ensemble to compute their respective conductances.

We estimate the uncertainty σ_G associated with the conductance by ablation. For each ensemble, we re-compute the conductance by omitting a single sAMC sample from the ensemble, and we repeat this operation for each structure in the ensemble. We then define the uncertainty in our estimate of the ensemble's conductance as follows:

$$\sigma_G = \max_n |G - G^{(n)}|,$$

where G is the conductance we obtained by including all structures in the ensemble in our calculation, and $G^{(n)}$ is the conductance obtained when omitting only the n^{th} structure from the percolation calculation.